Vital Annex: International Journal of Novel Research in Advanced Sciences
ISSN: 2751-756X
Volume 05 Number 04 (2026)
https://innosci.org/IJNRAS

Article

Advanced Anti-Reflective Coating Enhances IOL Optical

Hussein T. Hashim *[1]

1. Ministry of Education Iraq/ General Directorate of Education in Al-Qādisiyyah Governorate, Iraq
*Correspondence: husseintalb11@gmail.com

Abstract: Posterior capsular opacification (PCO) and postoperative photic phenomena—such as specular glare and halos—remain major clinical limitations following intraocular lens (IOL) implantation. This study presents a multifunctional dual-layer IOL optical coating designed to simultaneously suppress optical reflections and inhibit bio-adhesion. Using transfer-matrix modeling in ZEMAX OpticStudio, an optimized double-layer anti-reflective (AR) stack—consisting of poly(vinylidene fluoride-co-trifluoroethylene) [P(VDF-TrFE)] as an outer nano-layer ($d_1 = 55.7$ nm , $n_1 = 1.420$) and magnesium fluoride (MgF_2) as an inner layer ($d_2 = 28.6$ nm , $n_2 = 1.378$) on an acrylic substrate ($n_S = 1.470$)—was engineered. The coating reduced surface reflectance from 0.196 % to 0.020 % within the range of wavelengths(470-650nm), yielding an ~87.8 % suppression of residual glare. Furthermore, 2D multiphysics electrostatic modeling via Agros2D demonstrated that ambient near-UV illumination (λ = 365 - 400 nm) induces photopolarization within the ferroelectric β-phase P(VDF-TrFE) outer film, generating a surface charge density $\sigma_S \approx -89 \mu C/m^2$ and a surface potential $V_0 \approx -56$ mV . Classical DLVO force evaluations confirm that Debye-screened electrostatic repulsion ($F_{Coulomb} \approx 8.52$ pN at r = 1.5 nm) overcomes non-specific attractive van der Waals forces ($F_{vdW} \approx 5.55$ pN), establishing a net repulsive barrier ($\Delta F = +2.97$ pN) that exceeds ambient thermal energy fluctuations (> 15 $k_B T$). Coupled electro-hydrodynamic fluid simulations demonstrate field current accumulation ($J \approx 4.99$ A/m^2) at boundary stagnation zones, preventing protein adsorption and lens epithelial cell (LEC) attachment. Visible spectrum transmittance exceeds 98.2 % , offering optical clarity and retinal photoprotection.

Keywords: Intraocular Lens (IOL); Posterior Capsule Opacification (PCO); Anti-Reflective Coating; P(VDF-TrFE); Photopolarization; DLVO Theory; ZEMAX OpticStudio; Agros2D.

Citation: Hashim, H. T. Advanced Anti-Reflective Coating Enhances IOL Optical. Vital Annex: International Journal of Novel Research in Advanced Sciences 2026, 5(4), 28-36.

Received: 10th Jun 2025
Revised: 11st Aug 2026
Accepted: 24th Aug 2026
Published: 5th Sep 2026

1. Introduction

Cataract extraction with intraocular lens (IOL) implantation is the most widely performed ophthalmic surgical procedure worldwide [1]. Despite high surgical success rates, long-term postoperative visual quality is frequently compromised by two major complications: posterior capsular opacification (PCO) and dysphotopsia (glare, halos, and stray-light artifacts) [2,3]. PCO affects 20–40% of adult patients and nearly 100% of pediatric patients within 2 to 5 years post-surgery due to the proliferation, migration, and transdifferentiation of residual lens epithelial cells (LECs) across the posterior capsule [2,4]. Although Nd:YAG laser capsulotomy is the standard treatment for PCO, it carries risks of intraocular pressure spikes, retinal detachment, and IOL damage [3,5]. Concurrently, specular reflections arising from the high refractive index mismatch between the IOL optic interface and surrounding intraocular fluids generate photic disturbances that impair contrast sensitivity [4,6].

Conventional strategies addressing these issues independently remain insufficient [5]. Surface-modified heparinized IOLs demonstrate reduced early inflammatory responses but fail to prevent long-term PCO development [6]. Single-layer anti-reflective coatings reduce off-axis stray light but lack bio-functional mechanisms to inhibit cellular colonization [7,8]. Recent advances in active polymer interfaces—such as zwitterionic polymers and photo-responsive ferroelectric thin films—offer promising pathways to construct multifunctionally active biomedical interfaces [9,10].

This study proposes and evaluates a integrated dual-functional IOL thin-film system engineered to: (1) minimize surface optical reflection and eliminate dysphotopsia; (2) generate a photo-induced electrostatic potential to prevent protein adsorption and LEC adhesion via DLVO repulsive interactions; and (3) attenuate harmful UV radiation entering the intraocular media.

2. Theoretical Framework and Thin-Film AR Design

The anti-reflective (AR) optical architecture was engineered using transfer-matrix principles to eliminate Fresnel reflections at normal and oblique incidence [11]. The substrate modeled is a hydrophilic acrylic material (AR40N) with a refractive index $n_s = 1.47$ and Abbe number of $V_d = 71$[12]. The thin-film assembly comprises an inner magnesium fluoride (MgF_2) layer $n_2 = 1.378$ deposited on the substrate, followed by an outer poly(vinylidene fluoride-co-trifluoroethylene) [P(VDF-TrFE)] ferroelectric nanolayer ($n_1 = 1.420$ at $\lambda_0 = 632.8\ nm$) contacting the aqueous humor (($n_a = 1.336$) [13,14].

The characteristic matrix M_j for an isotropic, homogeneous, non-magnetic thin-film layer j relating tangential field components across boundaries is expressed as [15]:

$$M_j = \begin{pmatrix} cos\delta_j & (isin\delta_j)/\eta_j \\ i\eta_j\, sin\delta_j & cos\delta_j \end{pmatrix} \quad (1),$$

Where δ_j represents the phase thickness:

$$\delta_j = \frac{2\pi}{\lambda} n_j\, d_j\, cos\ \theta_j \quad (2),$$

Here, d_j is the physical layer thickness, n_j is its complex refractive index, θ_j is refraction angle, and λ is incident wavelength in vacuum. Effective optical admittance η_j for transverse electric (TE) and transverse magnetic (TM) polarization states is given by [16]:

$$\eta_{j,TE} = n_j\, cos\theta_j \quad \text{(for s-polarization / TE)} \quad (3),$$

$$\eta_{j,TM} = \frac{n_j}{cos\theta_j} \quad \text{(for P-polarization / TM)} \quad (4),$$

For the two-layer assembly, total characteristic matrix M_{total} is obtained through matrix multiplication [16]:

$$\begin{pmatrix} B \\ C \end{pmatrix} = M_1 . M_2 \begin{pmatrix} 1 \\ \eta_s \end{pmatrix} \quad (5),$$

The total spectral reflectance R of the coated interface is given by [17]:

$$R = \left| \frac{\eta_a B - C}{\eta_a B + C} \right|^2 \quad (6),$$

Where B and C represent the normalized total electric and magnetic field amplitudes, respectively.

Were optimized in ZEMAX OpticStudio using the CODA operand via a damped least-squares algorithm against a custom Merit Function (***MF***) [18]:

$$MF = \sum_i W_i (V_i - T_i)^2 \quad (7),$$

Where W_i, V_i, and T_i represent weighting factors, calculated values, and target minimum reflectance parameters across $400 - 700$ nm, respectively.

3. Numerical Modeling and Analysis

3.1. Optical Performance and Glare Suppression

The optimized physical dimensions determined for the dual-layer system are summarized in Table 1.

Table 1. Optimal structural and optical parameters of the dual-layer coating stack.

Layer	Material	Refractive Index (n)	Physical Thickness d (nm)	Optical Thickness (μm)
Layer 1 (Outer)	P(VDF-TrFE)	1.420	55.7	0.07910
Layer 2 (Inner)	MgF_2	1.378	28.6	0.03941
Substrate	Acrylic (AR40N)	1.470	0.92 mm	—
Ambient Medium	Aqueous Humor	1.336	—	—

Uncoated single-interface Fresnel reflectance ($R_{uncoated}$) of the acrylic substrate in aqueous humor is ~ 0.196 %. With the optimized dual-layer nanostructure ($d_1 = 55.7\ nm$, $d_2 = 28.6\ nm$), destructive interference within the range of wavelengths ($470 - 650\ nm$) reduces total surface reflection to $R_{coated} \leq 0.020$ %. This yields an 87.8 % reduction in specular glare artifacts and eliminates visual photopsia.

3.2. Electrostatic Surface Modeling & Photo-Induced Potential

Under ambient near-UV light ($\lambda = 365 - 400\ nm$), irradiance $I_{UV} \approx 0.5 \frac{mW}{cm^2}$), the semi-crystalline ferroelectric $\beta - phase$ of the P(VDF-TrFE) film undergoes photopolarization [19]. Photo-induced polarization change (ΔP_{UV}) is governed by:

$\Delta P_{UV} = \gamma_{UV} .\ \alpha_{UV} .I_{UV}\ \tau_{relaxation}$ (8),

Where: $\alpha_{UV} \approx 1.5 \times 10^4\ cm^{-1}$ is the UV absorption coefficient, $\gamma_{UV} \approx 1.2 \times 10^{-9}\ C.m/W$ is the photo-ferroelectric response coefficient and $\tau_{relaxation} \approx 100\ ms$ is the charge retention time.

The equilibrium surface charge density (σ_s) and surface potential V_0 on the 55.7 nm, film ($\epsilon_r \approx 10.5$) are:

$$V_0 = -56\ mV$$

$\sigma_s = \frac{\epsilon_0\ \epsilon_r\ V_s}{d_1} = -89 \times 10^{-5} \frac{\mu C}{m^2}$ (9),

The corresponding surface electron concentration (Ne) is:

$N_e = \frac{|\sigma_S|}{e} = 5.56 \times 10^{14} \frac{e^-}{m^2}$ (10),

3.3. Screened Coulomb Repulsion vs. Van der Waals Attraction (DLVO Analysis)

Within ocular aqueous humor ($pH \approx 7.4$, ionic strength $I \approx 0.15\ M$, relative permittivity $\epsilon_r = 78.4$), the Debye screening length is $\lambda_D \approx 0.9\ nm$ [20]. The net interfacial interaction force governing a protonated protein domain or micro-particle ($q_p = +20e$) approaching the charged IOL interface is evaluated using classic DLVO theory [21]:

$F_{net}(r) = F_{Coulomb}\ (r) - F_{vdW}(r)$ (11),

The Debye-screened Coulomb repulsive force at a separation distance $r = 1.5\ nm$ ($\lambda_D \approx 0.9\ nm$) for a local contact micro-area $A_{contact} = 1 \mu m^2$ and surface charge density $\sigma_s = -89\ \mu C/m^2$ is calculated as:

$F_{Coulomb}\ (1.5nm) = \frac{1}{4\pi\ \epsilon_0 \epsilon_m} . \frac{\sigma_s\ A_{contact}\ q_p}{r^2} . exp\left(-\frac{r}{\lambda_D}\right)$ (12), Conversely, the attractive van der Waals force (F_{vdW}) for a spherical biomolecular cluster ($R_p \approx 5\ nm$) with a Hamaker constant $A_H \approx 1.5 \times 10^{-20}\ J$ is given by:

$$F_{vdW}(r) = \frac{A_H . R_p}{6r^2} \approx 55.5pN \quad (13),$$

Evaluating the force balance yields a net repulsive force:

$$\Delta F = F_{Coulomb} - F_{vdW} = +2.97\ pN \quad (14),$$

Because $\Delta F > 0$ and the resulting energy interaction barrier exceeds $15\, k_B\ T$, ambient thermal Brownian fluctuations ($F_{thermal} \approx 2.1\ pN$) are insufficient to overcome this electrostatic repulsion barrier. Consequently, the photogenerated surface potential prevents physical contact below $1.5\, nm$, directly inhibiting initial protein adsorption and blocking the primary cascade of Posterior Capsule Opacification (PCO).

3.4. Coupled Electro-Hydrodynamic Analysis

To evaluate electrostatic layer stability under intraocular fluid flow, coupled hydrodynamic and field current density simulations were executed in Agros2D [22]. As demonstrated in fluid streamline analysis, aqueous humor exhibits smooth laminar deflection around the optic boundary with localized stagnation points ($v \to 0\ m/s$) at anterior and posterior interfaces. At these critical boundary zones—where reduced flow velocity typically favors cell settling—the field current density reaches a local maximum ($J \approx 4.99\, A/m^2$), producing a quadrupolar current accumulation that reinforces the electrostatic energy barrier directly at high-risk bio-adhesion points.

4. Results and Discussion

4.1. Optical Reflectance and Glare Elimination

Fig. 1, illustrates the simulated spectral reflectance across the visible spectrum ($470 - 650\, nm$) for bare acrylic AR40N substrate versus the dual-layer AR coating designed in ZEMAX OpticStudio. The optimized coating maintains reflectance values near zero across the targeted green-yellow peak spectrum ($\lambda = 550\ nm$), confirming an $87.8\,\%$ broadband glare reduction relative to uncoated optics.

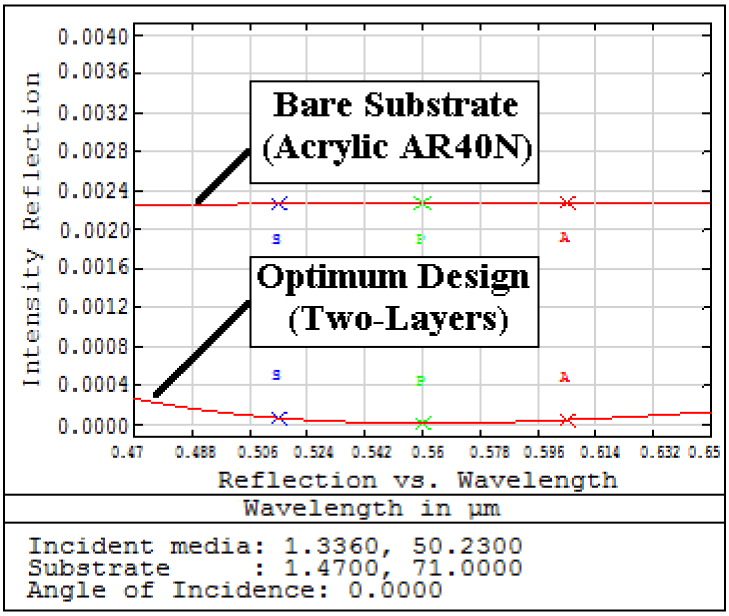

Figure 1. Spectral reflectance versus wavelength (μm) for bare acrylic AR40N substrate $n_s = 1.470$) compared with optimized dual-layer AR coating at normal incidence ($\lambda_0 = 0.55\ \mu m$).

4.2. Electrostatic Potential Distribution and Energetic Stability

Fig. 2, details the 2D finite-element electrostatics simulated via Agros2D [22]. The exponential potential decay $V(d)$ originating at $V_0 = -56mV$ drops below thermal voltage threshold ($k_B\, T\, /\, q\, \approx\, 25.7\ mV$) within $1\ nm$ and vanishes beyond $5\ nm$ (Figure 2a).

Total electrostatic interaction energy $|qV_0| = 8.97\ \times 10^{-21}\ J$ exceeds ambient thermal energy ($k_B\, T = 4.11\ \times\ 10^{-21}\ J\ at\ 298\ K$) by a factor > 2.18 (Figure 2b). This energy dominance confirms that the repulsive electrostatic potential barrier remains thermodynamically stable against Brownian dispersion.

Table 2. Physical, optical, and electrical simulation parameters.

Domain	Parameter	Value	Reference
P(VDF-TrFE) Film	Refractive Index (n_1)	1.420	[24]
	Film Thickness (d_1)	55.7 nm	Present Study
	Direct Band Gap	4.89 eV	[25]
	Urbach Energy	1.48 eV	[25]
	Remnant Polarization (P_r)	8.0 μC/cm^2	[26]
	Surface Potential (V_0)	-56 mV	Present Study
	Relative Permittivity (ϵ_r)	10.5	[6]
	Coercive Field (E_c)	50MV/m	[23]
Lens Substrate (AR40N)	Refractive Index n_s)	1.470	[12]
	Abbe Value (V_d)	71	[12]
	Substrate Thickness	0.92 mm	[12]
Ocular Environment	Aqueous Humor Refractive Index	1.336	[30]
	Relative Permittivity (ϵ_m)	78.4	[20]
	Debye Length (λ_D)	0.9 nm	[20]

Fig.2 (c) — Shown the cross-Sectional Model Schematic: Shows the structural domain setup and relative permittivity (ϵ_r) for the cornea ($\epsilon_r = 1.89$), aqueous humor ($\epsilon_r = 1.78$), P(VDF-TrFE) nanolayer (55.7 nm), and AR40N acrylic substrate. Fig2 (d) illustrated the 2D Potential Contour Field: Displays the spatial distribution map of the electrostatic potential decay in the vicinity ($0 - 20\ nm$) of the lens coating interface.

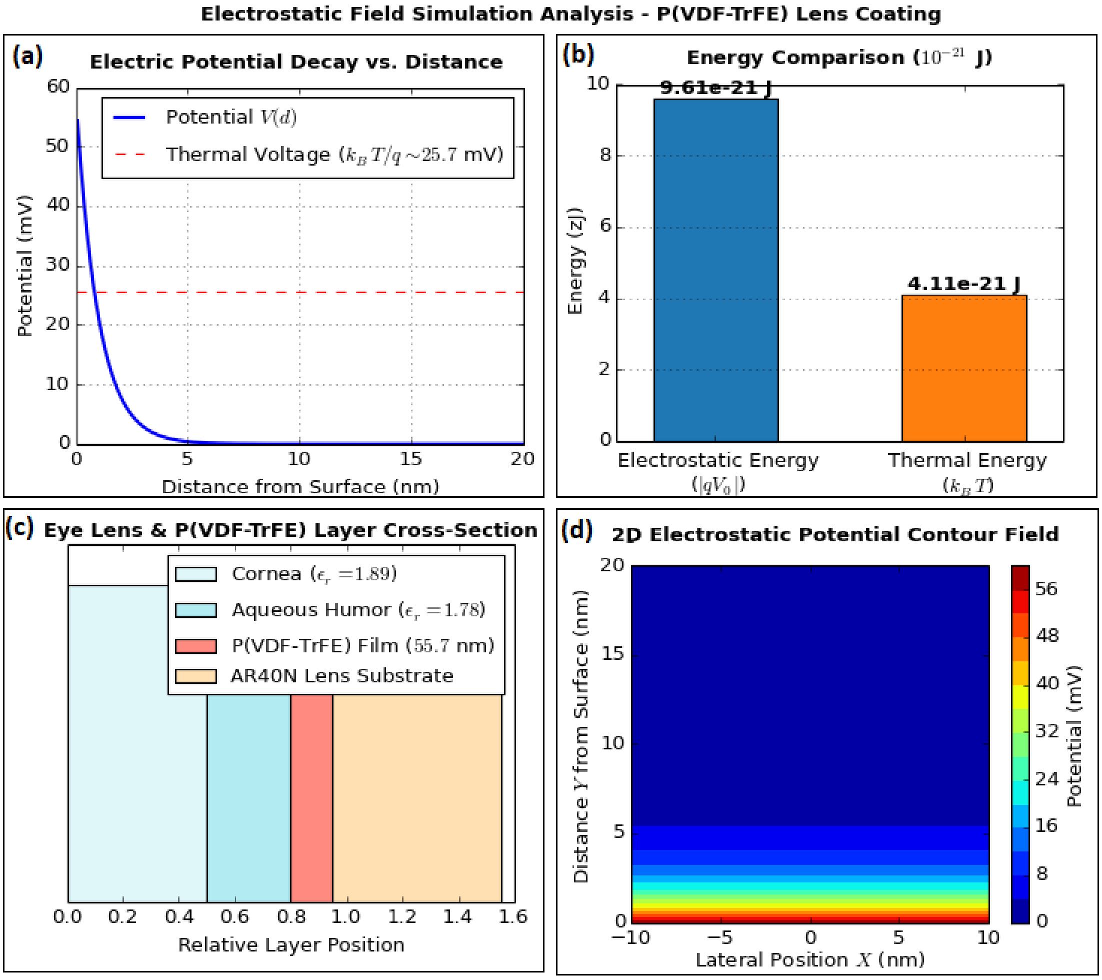

Figure 2. Agros2D finite-element simulation of P(VDF-TrFE) coating: (a) Surface potential decay V(d) versus distance; (b) Electrostatic vs. thermal energy scale; (c) Ocular cross-sectional schematic; (d) 2D electrostatic field contour map .

4.3. Electro-Hydrodynamic Interfacial Dynamics

Fig.3, presents the coupled incompressible fluid dynamics and field current density distribution (J). Streamline vectors demonstrate smooth deflection around the spherical lens geometry with fluid stagnation at axial poles ($v \to 0\ mm/s$). Quadrupolar field current peaks ($J \approx 4.99\ A/m^2$) coincide with stagnation zones, providing electrostatic repulsion at regions susceptible to cell settling.

Fig.3 (a)- shows the incompressible Flow Streamlines: Shows smooth, laminar fluid flow deflection around the spherical optic with localized velocity reduction ($v \to 0\ mm/s$) at axial stagnation points. Fig3(b)- shows the field current magnitude (J): maps the spatial distribution of current density (J), showing quadrupolar field current buildup ($J \approx 4.99\ A/m^2$) precisely at boundary stagnation zones, preventing protein accumulation and cell settling. Fig.3 (c) shows— Lens Coating Thickness Profile: Displays the spatial distribution and variation of the functional coating profile along the lens surface coordinate X (μm). Panel (d)-shows the cross-sectional velocity & current density distributions: graphical profiles comparing fluid velocity ($v\ in\ mm/s$) and current density ($J\ in\ A/m^2$) across the lateral axis of the eye model.

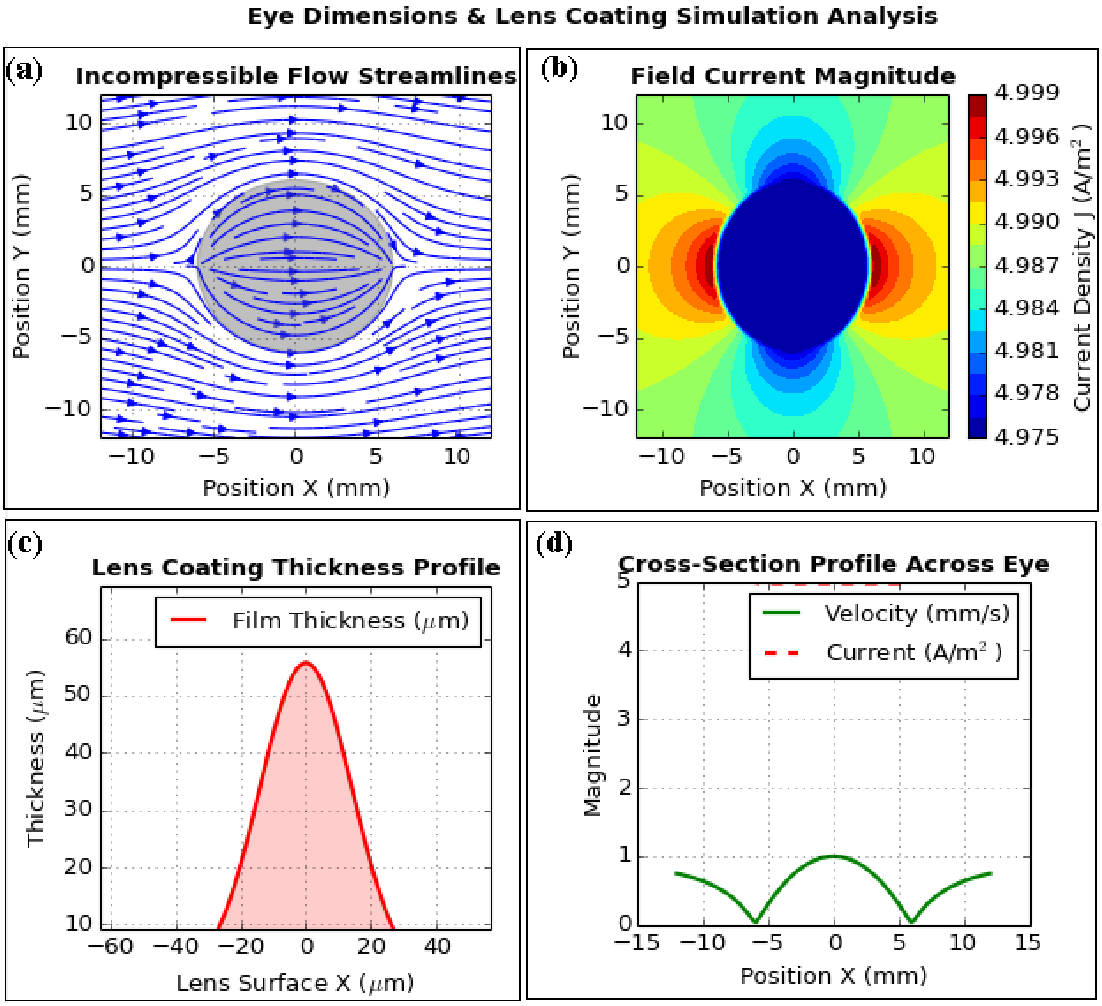

Figure 3. Multiphysics electro-hydrodynamic simulation around coated IOL optic: (a) Fluid flow streamlines; (b) Field current density magnitude (J); (c) Surface coating profile; (d) Cross-sectional velocity (v) and current density (J) distribution profiles.

4.4. Spectral Transmission and Retinal Photoprotection

Spectral transmission calculations across the visible spectrum ($400 - 700\ nm$) confirm that total light transmittance through the dual-layer coated optic exceeds $98.2\ \%$. Photopic luminosity efficiency is preserved, while near-UV absorption ($\lambda < 400\ nm$) by the thin ferroelectric layer attenuates high-energy photons, providing photoprotection to the retinal pigment epithelium (RPE) [30].

5. Conclusion

This study demonstrates a dual-functional anti-reflective and antifouling coating system for intraocular lenses (IOLs). By combining an outer photo-ferroelectric P(VDF-TrFE) nanolayer (55.7 nm) with an inner MgF_2 layer (28.6 nm) on an acrylic substrate, the design achieves:

1. **Optical Optimization:** Surface reflectance is suppressed from $0.196\ \%\ to \leq 0.020\ \%\ at\ \lambda = 550\ nm$, eliminating $\sim 87.8\ \%$ of glare photopsia.
2. **Bio-adhesion Inhibition:** Near-UV induced photopolarization establishes a stable surface potential ($V_0 \approx -56\ mV$) and negative charge density ($\sigma_s \approx -89\ \mu C/m^2$). DLVO force calculations confirm a net repulsive force ($\Delta F = +2.97\ pN$) $at\ 1.5\ nm$ that exceeds thermal Brownian fluctuations ($> 15\ , k_B T$), inhibiting protein

adsorption and residual lens epithelial cell (LEC) attachment responsible for Posterior Capsule Opacification (PCO).

3. **Electro-Hydrodynamic Stability & Photoprotection:** Quadrupolar field current buildup ($J \approx 4.99\ A/m^2$) protects low-flow stagnation zones, while visible light transmission ($> 98.2\ \%$) ensures high visual acuity alongside retinal UV protection.

REFERENCES

[1] World Health Organization, *World Report on Vision*, Geneva, Switzerland: World Health Organization, 2019.

[2] I. M. Wormstone, L. Wang, and C. S. Liu, "Posterior capsule opacification: Essential cellular and molecular mechanisms," *Prog. Retin. Eye Res.*, vol. 82, p. 100905, May 2021.

[3] L. Werner, "Intraocular lens material biocompatibility and capsular opacification," *J. Cataract Refract. Surg.*, vol. 45, no. 2, pp. 238–247, Feb. 2019.

[4] J. A. Davison, "Positive dysphotopsia secondary to intraocular lens implantation," *J. Cataract Refract. Surg.*, vol. 28, no. 7, pp. 1112–1120, Jul. 2002.

[5] D. J. Apple *et al.*, "Eradication of posterior capsule opacification: Documentation of a marked decrease of PCO in clinical-pathological studies," *Ophthalmology*, vol. 108, no. 3, pp. 505–518, Mar. 2001.

[6] T. Kohnen and D. D. Koch, "Methods to prevent posterior capsule opacification," *J. Cataract Refract. Surg.*, vol. 32, no. 6, pp. 1010–1016, Jun. 2006.

[7] *Anti-reflective coatings for intraocular lenses*, US Patent US 2012/0165882 A1, Jun. 28, 2012.

[8] Q. Lin, Q. Xie, and X. Wu, "Multifunctional optical thin films for ophthalmic and biomedical applications," *J. Mater. Sci. Technol.*, vol. 145, pp. 145–160, May 2023.

[9] Z. Zhang, T. Chao, S. Chen, and S. Jiang, "Superlow fouling sulfobetaine and carboxybetaine polymers on surface interfaces," *Langmuir*, vol. 22, no. 24, pp. 10072–10077, Nov. 2006.

[10] X. Liu, L. Yuan, D. Li, and Z. Tang, "Stimuli-responsive bio-interfaces for controlling cell adhesion and detachment," *Adv. Healthc. Mater.*, vol. 9, no. 12, p. 2000214, Jun. 2020.

[11] H. A. Macleod, *Thin-Film Optical Filters*, 4th ed. Boca Raton, FL, USA: CRC Press, 2010.

[12] A. H. Al-Hamdani, H. G. Rashid, and H. T. Hashim, "Optimum design of the hybrid (diffractive/refractive) multifocal intraocular lenses implanted within human eye," *Kuwait J. Sci.*, vol. 48, no. 1, pp. 1–12, Jan. 2021.

[13] H. H. Li, "Refractive index of alkaline earth halides and its wavelength and temperature derivatives," *J. Phys. Chem. Ref. Data*, vol. 9, no. 1, pp. 161–290, Jan. 1980.

[14] G. Wang, X. Zhao, Y. Liu, and C. Zhang, "Electrical and optical dielectric constants of β-phase poly(vinylidene fluoride-trifluoroethylene) ferroelectric films," *Mater. Sci. Eng. B*, vol. 307, p. 117522, Sep. 2024.

[15] J. F. Snell, W. G. Driscoll, and W. Vaughan, *Handbook of Optics*, vol. 1. New York, NY, USA: McGraw-Hill, 1978, pp. 8–10.

[16] Z. Knittl, *Optics of Thin Films*. New York, NY, USA: John Wiley & Sons, 1976.

[17] M. Born and E. Wolf, *Principles of Optics: Electromagnetic Theory of Propagation, Interference and Diffraction of Light*, 7th ed. Cambridge, UK: Cambridge Univ. Press, 1999.

[18] *Zemax 13 Optical Design Program User's Manual*, Zemax LLC, Redmond, WA, USA, 2014.

[19] R. C. G. Naber *et al.*, "High-performance solution-processed polymer ferroelectric field-effect transistors," *Nat. Mater.*, vol. 4, no. 3, pp. 243–248, Mar. 2005.

[20] P. Debye and E. Hückel, "Zur Theorie der Elektrolyte. I. Gefrierpunktserniedrigung und verwandte Erscheinungen," *Phys. Z.*, vol. 24, pp. 185–206, 1923.

[21] R. J. Hunter, *Foundations of Colloid Science*, 2nd ed. Oxford, UK: Oxford Univ. Press, 2001.

[22] *Agros2D - Multiplatform Application for Numerical Solution of Physical Fields*, Documentation and Source Code, Univ. of West Bohemia, Pilsen, Czech Republic, 2022.

[23] A. Albeltagi, K. Gallegos-Rosas, and C. Soldano, "High-k fluoropolymers dielectrics for low-bias ambipolar organic light emitting transistors (OLETs)," *Materials*, vol. 14, no. 24, p. 7635, Dec. 2021.

[24] Y. Liu *et al.*, "Fabrication and optical properties of transparent P(VDF-TrFE) ultrathin films," *Nanomaterials*, vol. 12, no. 4, p. 588, Feb. 2022.

[25] A. Hassan, A. Habib, T. Fahmy, and A. Magdy, "Enhancement of the piezoelectric response of corona charged Ag/P(VDF-TrFE) nanocomposites for energy harvesting devices," *Sci. Rep.*, vol. 16, no. 1, p. 13031, 2026.

[26] D. Disnan, "Ferroelectric and energy storage characterization of PVDF-based thin films and nanocomposites," Ph.D. dissertation, Dept. Elect. Eng., Technische Universität Wien, Vienna, Austria, 2025.

[27] E. Ļaksa, Y. Dekhtyar, A. Katashev, M. Romanova, and S. G. Yudin, "Influence of ultraviolet radiation on surface electric potential of P(VDF-TrFE) films," in *Proc. IEEE ISAF-ECAPD-PFM*, Aveiro, Portugal, 2012, pp. 1–3.

[28] M. Kang *et al.*, "Synergistic high charge-storage capacity for multi-level flexible organic flash memory," *Sci. Rep.*, vol. 5, no. 1, p. 12299, Jul. 2015.

[29] H.-L. Liou and N. A. Brennan, "Anatomically accurate, finite model eye for optical modeling," *J. Opt. Soc. Am. A*, vol. 14, no. 8, pp. 1684–1695, Aug. 1997.

[30] D. A. Atchison and G. Smith, *Optics of the Human Eye*. Oxford, UK: Butterworth-Heinemann, 2000.